Am J Transl Res 2021;13(10):11026-11047
www.ajtr.org /ISSN:1943-8141/AJTR0126967

*Original Article*

# Decellularized extracellular matrix loaded with IPFP-SC for repairing rabbit osteochondral defects

Lexiang Li*, Yi Chen*, Qiwei Fu*, Haishan Wu, Yiqin Zhou, Jiahua Shao, Jun Wu, Yaguang Han, Qirong Qian

*Department of Joint Surgery and Orthopedic Medicine, Changzheng Hospital, Naval Medical University, Shanghai 200003, China. *Equal contributors.*

Received November 24, 2020; Accepted April 12, 2021; Epub October 15, 2021; Published October 30, 2021

**Abstract:** Background: Tissue engineering is widely applied to treat osteochondral damage in osteoarthritis (OA). However, the superposition of seed cells, material scaffolds, inducing factors, and microenvironmental factors limit their practical application. We intended to develop a novel tissue engineering method for improving the repairment of osteochondral damage and to discuss its effect on repairing osteochondral defects. Methods: The combined decellularization methods of physics, chemistry and enzymes were used to decellularize rabbit rib cartilage and articular cartilage, and rabbit decellularizated osteochondral composite scaffolds were prepared. The structure and organization of the scaffolds were analyzed. We extracted and identified infrapatellar fat pad stem cells (IPFP-SCs) from healthy rabbits and OA rabbit, which were different in viability, migration, osteogenic and chondrogenic differentiation. Finally, a variety of decellularizated bone cartilage composite scaffolds were loaded with rabbit IPFP-SC for *in vitro* and *in vivo* studies. Results: The decellularization effect was strong, and the organic ingredients were lost. The layered scaffold showed lower density, greater porosity, larger pore size and water absorption than the whole scaffold, but the mechanical properties of the two scaffolds were low. IPFP-SCs were successfully extracted, and the migration and cartilage ability of IPFP-SCs in OA group were weak. The decellularized scaffold showed a high biocompatibility. The structure and composition of osteochondral promoted osteogenic differentiation and chondrogenic differentiation of IPFP-SCs. Moreover, the decellularized extracellular matrix loaded with IPFP-SC had the strongest repairing effect. Conclusion: The decellularized extracellular matrix loaded with IPFP-SC showed a better repair effect on rabbit osteochondral defects.

**Keywords:** Tissue engineering, osteoarthritis, decellularized extracellular matrix, infrapatellar fat pad stem cells, osteochondral defects

## Introduction

Osteoarthritis (OA) is a degenerative disease caused by many factors such as aging and joint deformities [1]. When the joint osteochondral is acutely damaged without a proper treatment, it will eventually develop into traumatic OA [2]. The main manifestations of OA are degenerative lesions of the hypochondral hyaline cartilage (HC), calcified cartilage (CC), and subchondral bone (SB) [3]. After losing the support or cushion of the osteochondral joints, the joints will quickly become fragile, releasing inflammatory factors and aggravating osteochondral damage [4]. Therefore, studying the repair of osteochondral damage is of great significance to reduce the incidence of OA and relieve the symptoms of OA patients.

Tissue engineering provides a new therapeutic direction for the treatment of OA osteochondral injury by mixing seed cells with various materials with high biocompatibility to form a cellular material complex, thus allowing seed cells to transform into target cells at the damaged site and secrete extracellular matrix (ECM) to replace the original organization [5]. Compared with traditional surgical wound repair methods, tissue regeneration has less damage, but high efficiency and curative effect [6]. Therefore, research on tissue engineering may be a promising method in the treatment of OA [6].

Seed cells, material scaffolds and inducing factors are the three elements of tissue engineering [7]. Stem cells are commonly used as seed cells in tissue engineering [8]. Mesenchymal

stem cells (MSC), which belong to pluripotent stem cells (PSC), are currently the most studied and potential seed cells for tissue engineering [9]. Among them, adipose-derived stem cell (ADSC) has many advantages such as more extensive tissue sources, faster expansion rate, slowing aging process, and long-term maintenance of stemness [9].

Recently, in tissue engineering, in addition to seed cells, scaffolds are used to load cells and provide temporary or permanent attachment and fixation sites for cells. The composition and structure of scaffolds also affect the differentiation of such daughter cells so that scaffolds become an indispensable part of tissue engineering [10, 11]. In addition to the three necessary elements of complete tissue engineering, the microenvironment in which the cells are located also plays an important role [11, 12]. Thus, avoiding antagonistic reaction when seed cells and materials are compatible is also a key point in selecting cell microenvironment in tissue engineering [13]. The immune response caused by human antigens mainly comes from cell membrane and cell nucleus [13]. Therefore, removing immunogenic cells while retaining the biologically active extracellular matrix (ECM) has become a new strategy for treating OA patients [14]. Decellularized extracellular matrix (dECM) is isolated extracellular matrix of tissues from its original inhabiting cells, which has emerged as a promising natural biomaterial for tissue engineering, aiming at support, replacement or regeneration of damaged tissues [15]. dECM can effectively capture complex arrays of proteins, glycosaminoglycans (GAG), proteoglycans and many other matrix components found in natural tissues [16, 17]. dECM is widely used in tissue engineering for its low antigenicity, bionic composition and structure, high biocompatibility, hydrophilicity, and biomechanical properties [18].

This study applied improved physical-chemical-enzyme combined decellularization methods to decellularize rabbit rib cartilage and articular cartilage to prepare rabbit decellularized osteochondral whole and stratified scaffolds. From healthy rabbits and OA rabbit, we extracted healthy rabbit and OA rabbit infrapatellar fat pad stem cells (IPFP-SC), and compared their proliferation, migration and chondrogenic differentiation. Finally, a variety of decellularized osteochondral composite scaffolds were loaded with rabbit IPFP-SC *in vitro* and *in vivo*.

In this study, the combined decellularization method was used to decellularize the osteochondral scaffold as a whole. Innovative use of rib cartilage instead of articular cartilage as a material source confirmed that there was no significant difference in structure, composition, physical parameters, biomechanics, or final repair of osteochondral defects, suggesting that rib cartilage can replace articular cartilage for tissue engineering material construction.

## Materials and methods

### *Ethics statement and animals*

Animal experiments were approved by the Animal Ethics Committee of Nanfang Hospital (DO201508003). The animal breeding was conducted at the Animal Experiment Center of Nanfang Hospital. Healthy New Zealand white rabbits (normal grade, male, 5-6 months old, weight: 2.5-3.0 kg) were purchased from Songlian Experimental Animal Base in Songjiang District, Shanghai, China (production license number: SCXK 2017-0008). Healthy BALB/c mice (specific pathogen free (SPF) grade, male, 2-3 months old, and weight: 20-30 g) were provided by Shanghai Jiesjie Experimental Animal Co., Ltd. (production license number: SCXK 2013-0006).

### *Fabrication of decellularized joints and rib cartilage integral scaffolds*

New Zealand white rabbits were anesthetized by intravenous injection of pentobarbital sodium 30 mg/Kg into ear vein. Following procedures were carried out after we observed that the rabbit corneal reflex disappeared, the respiratory rate dropped to about 12-14 beats/min and the rabbit thigh muscle deep reflex disappeared. After the skin preparation on the knee joints and the middle section of the breastbone, the white rabbit was stretched and fixed on an operating table in supine position. After routine disinfection and draping, the middle section 0.5 cm next to the patella of the rabbit's knee joint was positioned and incised to expose the joint capsule. Subsequently, the medial arteriovenous branch of the suprapatellar sac inside and above the subpatellar fat pad was found. By avoiding this branch from below,

the nodular sac was cut to expose the middle of the femoral trochlear. Finally, the osteochondral blocks were collected and put into sterile normal saline (S0817, Sigma-Aldrich, USA) for later use. The rabbits were washed with normal saline and sutured layer by layer.

The rabbit rib cartilage was collected as previously described [19]. Briefly, the 6-7 rib junctions of the rabbit were collected after exposing the joint of the sternum and ribs. The intercostal muscles and vascular nerves were stripped. Subsequently, the junction of the ribs and cartilage was exposed. The rib cartilage was then cut, taken out, and put in sterile saline for use. The rabbit was washed with saline and sutured layer by layer.

Approximately 1 hour (h) after bandage fixation, the rabbit was intramuscularly injected with penicillin sodium (Shandong Lukang Pharmaceutical Co. Ltd., China) at a dose of 150,000 U/Kg, and the rabbit was placed in a cage until full recovery. Antibiotics were given to prevent infection before operation, and anti-inflammatory and analgesic interventions were given after operation.

*The overall decellularization of rabbit articular cartilage and rib cartilage*

The rabbit joint osteochondral and rib cartilage complexes were washed and placed in a refrigerator at -80°C for 8 h. The composite was then placed in a 37°C oven to be completely melt, and ultrasonic cleaning was performed again (KQ5200DE, Kunshan Ultrasonic Instrument Co. Ltd., China), followed by repeated freezing for three times and vacuum freeze-drying for 24 h (FD-1A-50, Beijing Boyikang Experimental Instrument Co. LTD, China). The osteochondral complex was washed with phenylmethylsulfonyl fluoride (PMSF, 52332, Sigma-Aldrich) and Tris-HCL (PHG0002, SAFC, USA) at 4°C for 24 h by shaking, and then washed with 1% TritonX-100 at 4°C for 48 h, followed by the addition of 4% sodium deoxycholate solution (D6750, Sigma-Aldrich, USA) and shaking for 24 h. Next, the osteochondral complex was digested by DNase (DN25, Sigma-Aldrich, USA) and RNase (R6513, Sigma-Aldrich, USA) overnight at 37°C. After 72 h of immersion in deionized water, the osteochondral complex was frozen at -80°C for 48 h and then immediately placed in a FD-1A-50 vacuum freeze dryer for 24 h. The dried decellularized osteochondral complex was sterilized by low-temperature plasma irradiation for use. The last step in the decellularization process of the three-layer structure of rabbit joints and rib cartilage was replaced by crushing and disinfection.

Decellularized joint and rib cartilage-derived layered osteochondral scaffold were prepared. Briefly, 80 μL SB, 15 μL CC and 20 μL HC were added to the joints in sequence, frozen at -80°C for 15 minutes (min), and dried in a vacuum freeze dryer for 24 h. After 248 nm UV irradiation for 24 h, the stent was cross-linked with NHS/EDAC solution (H109330/N191699, Aladdin, China) at 37°C for 24 h, dialyzed for 24 h, vacuum freeze-dried and finally performed with plasma disinfection at low temperature.

*Histological staining analysis*

Hematoxylin-Eosin staining (HE): The sections were immersed and dewaxed in xylene (YZ-1601849, Solarbio, China) for 15 min, soaked in 100% ethanol (E7023, Sigma-Aldrich, USA) for 5 min, distilled with 80% ethanol for 5 min, followed by staining with hematoxylin aqueous solution (H8070, Solarbio, China) for 5 min and then dyeing with 1% eosin dye solution (G1100, Solarbio, China) for 2 min. After gradient alcohol dehydration and soaking in xylene, the sections were sealed with neutral gum and observed under a microscope (DM1000 LED, Leica, Germany).

Safranin solid green dyeing: The sections were stained with hematoxylin aqueous solution for 8 min, immersed first in distilled water for 5 min, then in the working solution of the solid green dye (RBG1058, Roles-Bio, China) for 3 min, and finally in the working solution of safranine (RBG1058, Roles-Bio, China) for 6 min.

Sirius scarlet stain: The sections were soaked in lapis lazuli blue solution for 8 min. After immersing the sections in Sirius-picric acid dye solution (RBGP1022, Roles-Bio, China) for 25 min, the sections were stained with hematoxylin aqueous solution for 5 min. The remaining treatments were the same as HE staining.

Toluidine blue staining: The sections were immersed in 0.5 toluidine blue staining solution (RBGP1028, Roles-Bio, China) for 30 min and then stained by glacial acetic acid for 1 min. The remaining treatments were the same as HE staining.

*High-resolution scanning electron microscope observation*

The natural osteochondral tissues were completely immersed in 4% paraformaldehyde (C104190, Aladdin, China), fixed for 4 h, dehydrated with gradient alcohol, then placed at -80°C for 4 h, and finally vacuum freeze-dried for 24 h. The dry decellularized monolith and layered scaffolds were subjected to conventional ion spray gold (30 s) and then observed under an electron microscope (SEM) (ULTRA 55, ZEISS-GEMINI, Germany).

*DNA content analysis*

A total of 9 types of microparticle supernatants were prepared using the three-layer structure of natural joint osteochondral, decellularized joints and rib cartilage, and then the same proportion of Hoechst33258 (HY-15558, MCE, USA) working solution was added. The optical density (OD) value was measured at the excitation wavelength of 550 nm using PLUS 384 microplate reader (Molecular Devices, USA).

*Joint and rib decellularized osteochondral matrix component detection*

The measurement of glycosaminoglycans (GAG) in the tissue was carried out using the 1, 9-Dimethyl-Methylene Blue (DMMB) colorimetric method (341088, Sigma-Aldrich, USA), and the OD value was measured at an excitation wavelength of 525 nm. A fully automatic amino acid analyzer (L-8900, Hitachi, Japan) was used for amino acid analysis. The dry particles of the CC and SB layers of the rabbit natural, decellularized joints and ribs were heated to obtain the carbonized specimens for testing. The difference in quality before and after carbonization was calculated to obtain mass and percentage of organic matter. The carbonized specimen was crushed to a fine powder and added to an X-ray diffractometer for analysis (XRD-6100, Shimadzu, Japan).

*Related physical parameters and biomechanical analysis of various decellularized osteochondral scaffolds*

The decellularized osteochondral scaffold was weighed, and the mass water absorption, volume density, true density, effective porosity and absolute porosity were calculated and analyzed. The decellularized osteochondral scaffold was made into 2 slices in parallel in the sagittal plane, and the slices were observed according to SEM scanning. The maximum diameter of all holes was measured from 5 random fields under a microscope to calculate and analyze the difference in the diameter of the articular cartilage and subchondral bone area. Interface sensors (MB, USA) were used for the biomechanical analysis of whole decellularized bone cartilage and layered scaffolds. The ZETA potential particle size analyzer (NICOMP380ZLS, PSS, USA) was used to analyze the particle size.

*Isolation and identification of IPFP-SC*

An OA rabbit model was established based on a previous literature [20]. Three months after the operation, the rabbits were sacrificed to extract the OA rabbit IPFP-SCs. The IPFP was removed and rinsed gently, cut into a paste, and then added with 0.2% type I collagenase solution (Coll I, C1-BIOC, Sigma-Aldrich, USA) at 37°C for 60 min. After centrifugation and removal of the supernatant, the pellet was resuspended in F12 complete medium (30-2006, ATCC, USA) and routinely cultured.

For flow cytometry (FC), IPFP-SC P3s were resuspended at a concentration of $10^5$/mL. CD34 (100 μg, GTX75441, USA, GeneTex), CD45 (25 μg, GTX116018, USA, GeneTex), CD73 (1:100, 560847, USA, BD), CD90 (50 μg, ab226, USA, Abcam), CD105 (50 μg, GTX11415, USA, GeneTex), and HLA-DR (0.1 mg, 555559, USA, BD) with fluorescein antibody were used for direct labeling. CytoFLEX flow cytometry (Beckman Coulter, USA) was used for monitoring analysis.

For immunofluorescence (IF) technology detection, IPFP-SCs were fixed with 4% paraformaldehyde for 20 min, permeabilized with 0.2% Triton X-100 (10789704001, Sigma-Aldrich, USA) for 30 min, and blocked with goat serum (G9023, Sigma-Aldrich, USA) at 37°C for 30

**Table 1.** Primers

| Gene | Sequences (5'-3') | Length |
|---|---|---|
| RUNX2 | Sense: TCCGAAATGCCTCTGCTGTTA | 171 bp |
| | Antisense: GGGGTCCATCCACTGTAACTTT | |
| ALP | Sense: AAACCCTTCACTGCCATCCTG | 106 bp |
| | Antisense: CCTGGTAGTTGTTGTGAGCGT | |
| SOX9 | Sense: AGCAAGAACAAGCCCCACGTC | 265 bp |
| | Antisense: CCTGCCCATTCTTCACCGACT | |
| ACAN | Sense: CATCTGGAGTTCTTTTTGGGAG | 122 bp |
| | Antisense: CAGGTCAGGGATTCTGTGTGTC | |
| COL2A1 | Sense: GAAGACACCAAGGACTGCCTG | 227 bp |
| | Antisense: GCACCCTTTTCGCCTTTGTCA | |
| GAPDH | Sense: CCGCCCAGAACATCATCCCT | 262 bp |
| | Antisense: GCACTGTTGAAGTCGCAGGAGA | |

min. The primary antibodies of CD44 (100 μg, GTX15883, USA, GeneTex), CD90, Coll-I (50 μL, ab6308, USA, Abcam) and Coll-II (500 Ml, 5B2.5, USA, NOVUS) were added and incubated with the cells overnight at 4°C. The cells were further incubated with fluorescent secondary antibody at 37°C in the dark for 1 h. Cell nuclei were stained by 4',6-Diamidino-2-phenylindole dihydrochloride (DAPI) (D9542, Sigma-Aldrich, USA) in the dark for 5 min.

*Identification of viability, migration, and osteogenic, adipogenic, and chondrogenic differentiation of IPFP-SCs*

Alizarin Red Staining (TMS-008, Millipore, USA) was performed to detect osteogenic differentiation of IPFP-SC. Oil Red O (90358, Millipore, USA) was used for adipogenic differentiation detection, and toluidine blue staining was employed to analyze the chondrogenic differentiation. Cell counting kit-8 (CCK-8) method (CK04, Solarbio, China) was applied to analyze the activity of IPFP-SC, and the absorbance was measured at OD 450 nm. Cell migration ability was determined by wound-healing experiment. The precipitation micelle method was used to induce OA and healthy rabbit IPFP-SC P3 to differentiate into chondrocytes and secrete cartilage matrix to form cartilage globules. Then the shape and size of the two cartilage globules were compared [21]. The mRNA expressions of RUNX family transcription factor 2 (RUNX2), alkaline phosphatase (ALP), SOX9, aggrecan (ACAN), and COL2A1 were determined by real-time quantitative PCR (RT-qPCR) [RT-PCR kit (KR123, TIANGEN, China), FastFire qPCR PreMix (FP207, TIANGEN, China)], and the primer sequences are shown in **Table 1**.

*Biocompatibility of rabbit decellularized osteochondral matrix with scaffolds*

Cell seeding: IPFP-SCs ($5 \times 10^6$/mL) were added to the decellularized joints and rib cartilage section and cultured for about 2 h, and then complete medium was added to culture for 48 h.

Stent inoculation: BALB/c mice were anesthetized by intraperitoneal injection of sodium pentobarbital 45 mg/kg. After we observed that the mice's limbs were weak without activity, the corneal reflex disappeared, and the breathing rate stably dropped to about 10-12 times/min, the following procedures were performed. A cavity (5 mm × 5 mm × 5 mm) was exposed on the back of BALB/c mice. The prepared whole articular cartilage, integral costal cartilage and articular cartilage layered scaffold were respectively put into the cavity, which was then washed with normal saline and sutured layer by layer.

Direct contact method between decellularized particles and IPFP-SC: The 6 prepared aseptic joints particles HC, CC, SB and rib particles HC, CC, SB were put into the IPFP-SC cell suspension ($1 \times 10^4$ cells/mL) and evenly pipetted. They were then added to a 12-well plate and cultured for 48 h.

*Establishment of rabbit femoral trochlea osteochondral defect model*

Rabbit anesthesia, skin preparation, disinfection, draping, and partial exposure of the femoral pulley were performed in the same way as before. We used a 5 mm diameter trephine (Cowtail Medical Technology (Suzhou) Co., Ltd., China) to drill a hole in the center of the trochlea to form an osteochondral defect.

*Decellularized osteochondral scaffolds models with implanted osteochondral defect*

After washing the articular cavity of the rabbit knee joint, each group of decellularized osteochondral stents with or without IPFP-SCs were placed. After observing that the cartilage surface of the stent was parallel to the pulley, the knee joint of the rabbit was sutured layer by

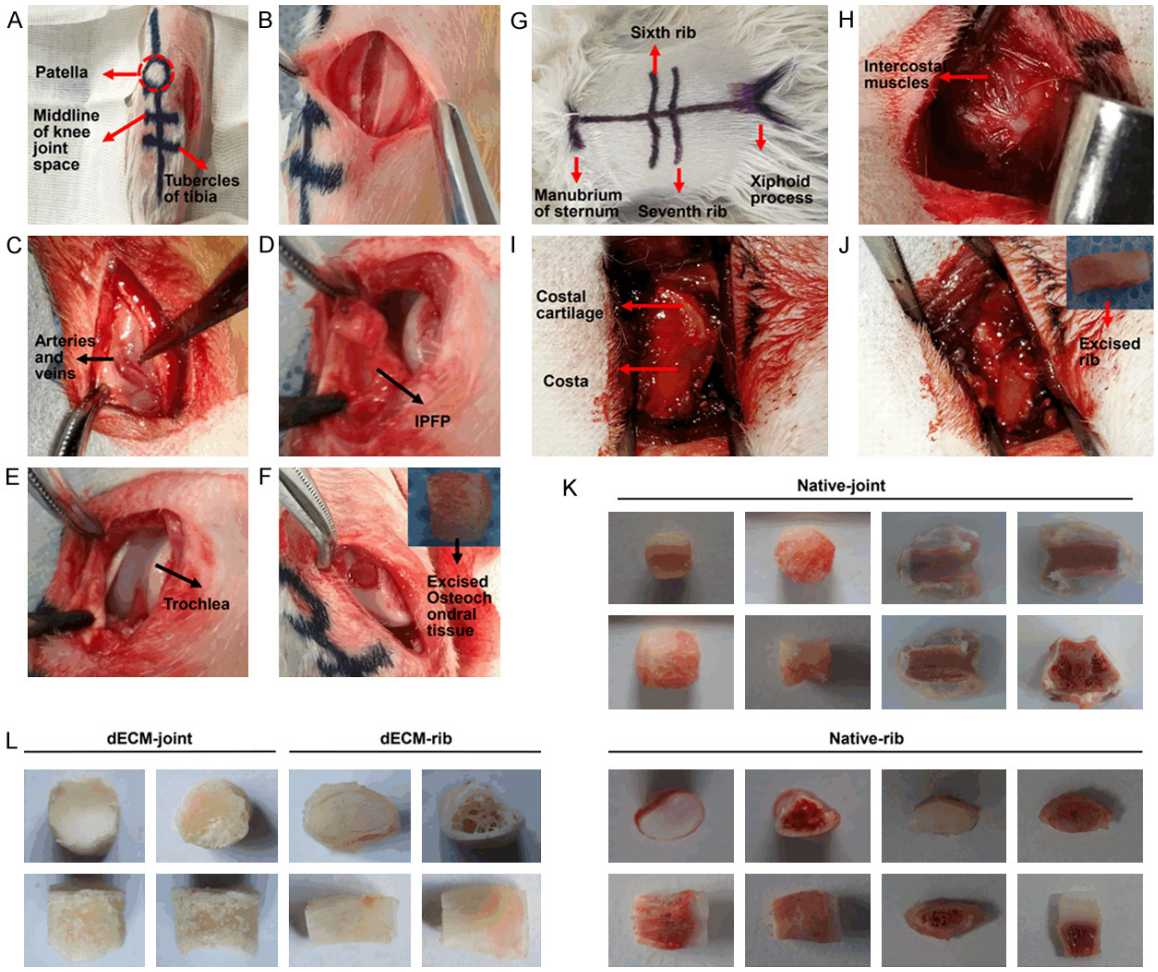


**Figure 1.** The overall removal process and structure diagram of rabbit knee joint osteochondral and rib cartilage. A. Schematic diagram of the internal incision and preparation of the rabbit knee joint. B. The skin and subcutaneous layers were incised. C. Attention was paid to avoid opening and closing the blood vessels and their branches inside the nodular sac. D. Picture of entering the joint capsule. E. The femoral pulley part was exposed. F. The bone cartilage in the middle of the pulley was drilled with a ring drill. G. Schematic diagram of arc-shaped incision and scoring of rabbit ribs. H. The skin and subcutaneous layers were incised to expose the intercostal muscles. I. The intercostal muscles were stripped to expose the rib cartilage. J. The rib cartilage was removed. K. The general view and three-layer structure of natural joints and rib cartilage. L. General view of decellularized joints and rib cartilage.

layer and wrapped with a bandage. 6 months after the operation, the experimental rabbits were sacrificed after deep anesthesia with pentobarbital for collecting the rabbit femoral trochlear specimens. The specimens were fixed with 4% paraformaldehyde after observation and photographing.

*Data analysis*

Statistical analysis was performed using SPSS 19.0. Biology and technology were repeated at least three times. The data were expressed as mean ± standard deviation. The comparison between the two groups was performed by independent sample *t*-test. The comparison between groups was performed by one-way analysis of variance, followed by Tukey's post hoc test. The difference was statistically significant with $P < 0.05$.

## Results

*Preparation of decellularized joint and rib cartilages holistic scaffolds*

As shown in **Figure 1A-J**, the whole bone cartilages of natural rabbit joints and rib were collected. The removed rabbit articular cartilage was a cylinder with a diameter of about 5 mm

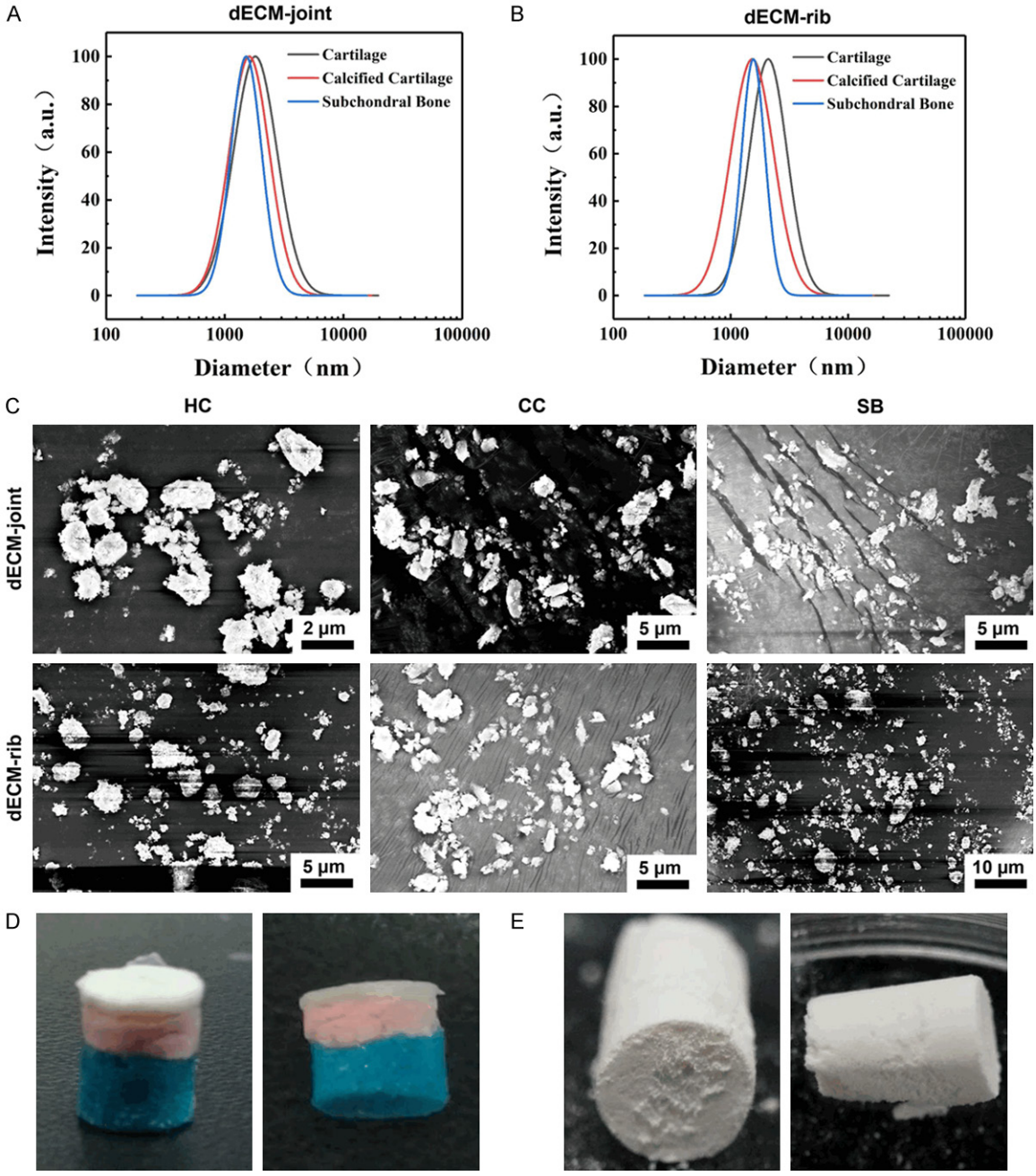


**Figure 2.** Fabrication of layered scaffolds for decellularized joints and rib cartilage. A. Size distribution of decellularized particles in rabbit joints. HC: Hyaline cartilage; CC: Calcified cartilage; SB: Subchondral bone. B. The size distribution of rabbit rib decellularized particles. C. SEM scan of decellularized hyaline cartilage, calcified cartilage and subchondral bone particles in rabbit joints and ribs. SEM: scanning electron microscope. D. Schematic model of layered osteochondral scaffold. E. Dry layered osteochondral scaffold.

and a height of 5 mm, while the rib cartilage was a slightly bent cylinder with a diameter of about 4 mm and a height of 5 mm. The three-layer structure was clearly different (**Figure 1K**). After the intact joint osteochondral and rib cartilage were decellularized and dried, three-layer structure of the two was well preserved without fracture or delamination (**Figure 1L**). The three-layer structure of joint and rib cartilage HC, CC, and SB had particle sizes between 1.5-2.5 μm without significant difference ($P > 0.05$, **Figure 2A**, **2B**). Such results were consistent with the

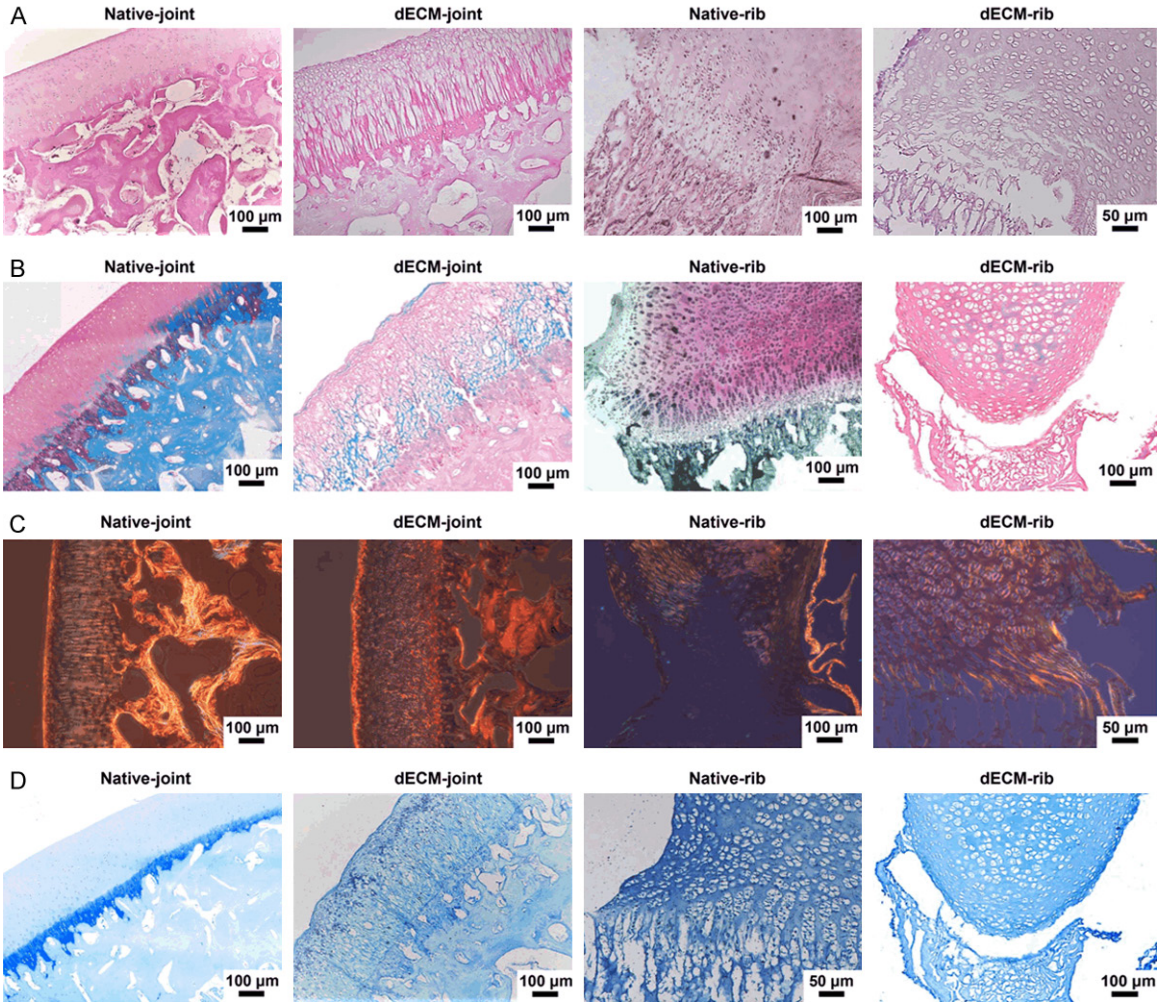


**Figure 3.** Histological staining of the whole joint and rib cartilage after decellularization. A. Hematoxylin-eosin (HE) staining image of natural articular cartilage, decellularized articular osteochondral, normal rib cartilage, and decellularized rib cartilage. B. Safranin-fast green staining images of four groups of cartilage. C. Sirius scarlet staining image of four groups of cartilage. D. Toluidine blue staining of cartilage in four groups.

particle diameter observed under a scanning electron microscope (**Figure 2C**). Subsequently, decellularized osteochondral scaffolds from different sources were successfully fabricated. The layered osteochondral scaffold model and the dried layered osteochondral scaffold were shown in **Figure 2D**, **2E**.

*Validation of decellularization effect of whole joint and rib cartilages*

To verify the decellularizing effect of joint and rib cartilage particles, histological staining was performed. The results showed that the three-layer structure of HC, CC and SB in natural joint osteochondral and rib cartilage could be distinguished, and the cartilage surface was smooth and complete (**Figure 3A-D**). The results of HE staining demonstrated that the cartilage surface in the decellularized articular cartilage was relatively complete, but it was unsmooth, uneven, and the CC layer was clear (**Figure 3A**). In the decellularized rib cartilage, the CC layer was fuzzy, and there was delamination and peeling (**Figure 3A**). Safranin-fast green staining results showed the blue staining of the HC layer of decellularized joint bone and rib cartilage, while SB showed red staining, and some cells were fused and expanded (**Figure 3B**). In Sirius staining, the structures of the decellularized articular cartilage and decellularized rib cartilage were disordered, and the refractive index of the three-layer structure was decreased to various degrees (**Figure 3C**). Additionally, toluidine blue staining did not show cells or cell debris in the decellularized joint bone or rib cartilage (**Figure 3D**).

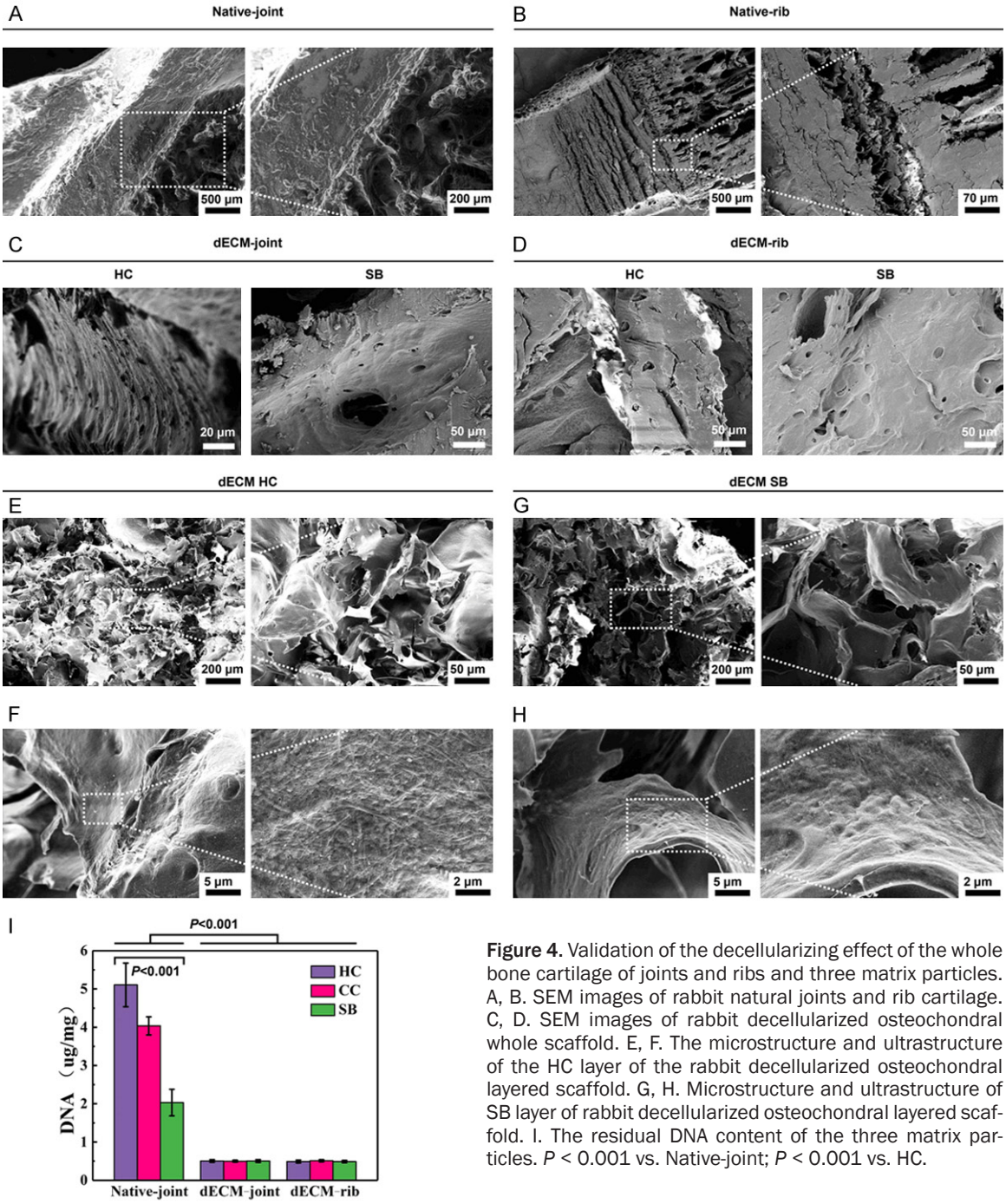


**Figure 4.** Validation of the decellularizing effect of the whole bone cartilage of joints and ribs and three matrix particles. A, B. SEM images of rabbit natural joints and rib cartilage. C, D. SEM images of rabbit decellularized osteochondral whole scaffold. E, F. The microstructure and ultrastructure of the HC layer of the rabbit decellularized osteochondral layered scaffold. G, H. Microstructure and ultrastructure of SB layer of rabbit decellularized osteochondral layered scaffold. I. The residual DNA content of the three matrix particles. $P < 0.001$ vs. Native-joint; $P < 0.001$ vs. HC.

Similarly, the SEM observation results verified the effect of decellularization of the whole joint and rib cartilage, and it could be seen that there were no cells in the cell cavity in the HC or SB tissues, and there were larger Haval tubes in the bone tissues (**Figure 4A-H**). In addition, we determined the DNA content of the three-layer structure particles after cartilage decellularization, and the results showed that the DNA content was decreased significantly ($P < 0.001$, **Figure 4I**).

*Detection of matrix components in acellular joints and costal cartilage*

Subsequently, the components of the decellularized joint and rib cartilage matrix were detected. In the same type of osteochondral

tissues, the content of GAG was the highest in HC and the second highest in CC, while the content of SB was the lowest. GAG content in decellularization was less than that in normal tissues ($P < 0.001$, **Figure 5A**). The amino acid content of HC, CC and SB of normal joint bone and decellularized joint osteochondral were shown in **Figure 5B**, **5C**. In addition, the content of CC inorganic matter in normal or decellularized osteochondral was less than that in SB, and the content of organic matter was more than that of the SB layer. The content of inorganic matter after decellularization was more than that of natural tissues, and the content of organic matter was less than that of normal tissues (**Figure 5D**).

*Determination of physical parameters of decellularized whole and stratified osteochondral scaffolds*

Next, we detected the physical parameters of the whole decellularized and layered osteochondral scaffolds. The bulk density of the integral stent was larger than that of the layered stent ($P < 0.001$, **Figure 5E**). Compared with the layered scaffold, the effective porosity and absolute porosity of the integral scaffold were smaller ($P < 0.001$, **Figure 5F**). The mass water absorption rate was obviously lower in the overall stent than the layered stent ($P < 0.001$, **Figure 5G**). In terms of pore size, the decellularized monolithic scaffold HC was the smallest, followed by the decellularized monolithic scaffold SB, and the layered crosslinked articular cartilage and subchondral bone were the largest ($P < 0.001$, **Figure 5H**).

*Isolation and identification of rabbit IPFP-SC, and the differentiation of adipogenesis, osteogenesis, and chondrogenesis*

To examine the effect of the bionic three-dimensional structure and normal components of the acellular osteochondral scaffold on the osteogenic and cartilage induction of IPFP-SC, we isolated and extracted rabbit IPFP-SCs (**Figure 6A**). Subsequently, as shown in **Figure 6B**, IPFP-SCs were subcultured. Then, flow cytometry and immunofluorescence staining were performed to identify IPFP-SCs. The expressions of CD90, CD105, CD73, CD44 and CD90 were higher in IPFP-SCs, and the expressions of HLA-DR, CD45 and CD34 were inhibited (**Figure 6C-E**). Histological staining experiments demonstrated that IPFP-SCs can be induced to produce calcium nodules, lipid droplets or cartilage globules (**Figure 7A-F**). There was no statistical difference in cell viability between OA rabbit and healthy rabbit IPFP-SCs (**Figure 8A**, **8B**), but the migration and chondrogenic differentiation of OA IPFP-SC was lower than that of healthy IPFP-SC (**Figure 8C-E**).

*Biocompatibility and biotoxicity of acellular osteochondral matrix and scaffold in rabbits*

To determine the biocompatibility of rabbit acellular osteochondral matrix and scaffold, we used three different inoculation methods. The P3 generation cells of IPFP-SC were seeded onto the integral scaffold of acellular osteochondral joints and ribs. SEM showed that on the HC and SB surfaces of the joints and ribs, the cell well survived, extending synapses, interconnected, intertwined into clusters, secreted extracellular matrix and surrounded the cells (**Figure 9A**). In the stent inoculation method, the three groups of mice were healthy, and the incisions healed well. Moreover, from the surface observation, there was no redness, swelling or rupture, no abnormal exudation, and the stent showed no change in size (**Figure 9B**). The method of direct contact between decellularized particles and IPFP-SC demonstrated that the adherent growth of the cells was not affected, and the cell shape and size were normal, without abnormal apoptotic cells (**Figure 9C**). In the extracts obtained from the two decellularized osteochondral scaffolds with different weight/volume ratios and different immersion days, there was no significant difference in IPFP-SC cell viability ($P > 0.05$, **Figure 9D**, **9E**).

*In vitro induction of rabbit acellular osteochondral matrix and scaffold with IPFP-SCs*

Immunofluorescence was used to determine the effect of decellularized particles on the secretion of Coll-I and Coll-II by IPFP-SC. The levels of Coll-I and Coll-II were significantly increased during the induction of osteogenic or chondrogenic fluid and decellularized particles (**Figure 10A**). Subsequently, we determined the expression of molecular markers to reflect osteogenic differentiation and chondrogenic differentiation. The results showed that the expression of ALP was significantly higher in group B, I-SB, and S-SB, and that the expres-

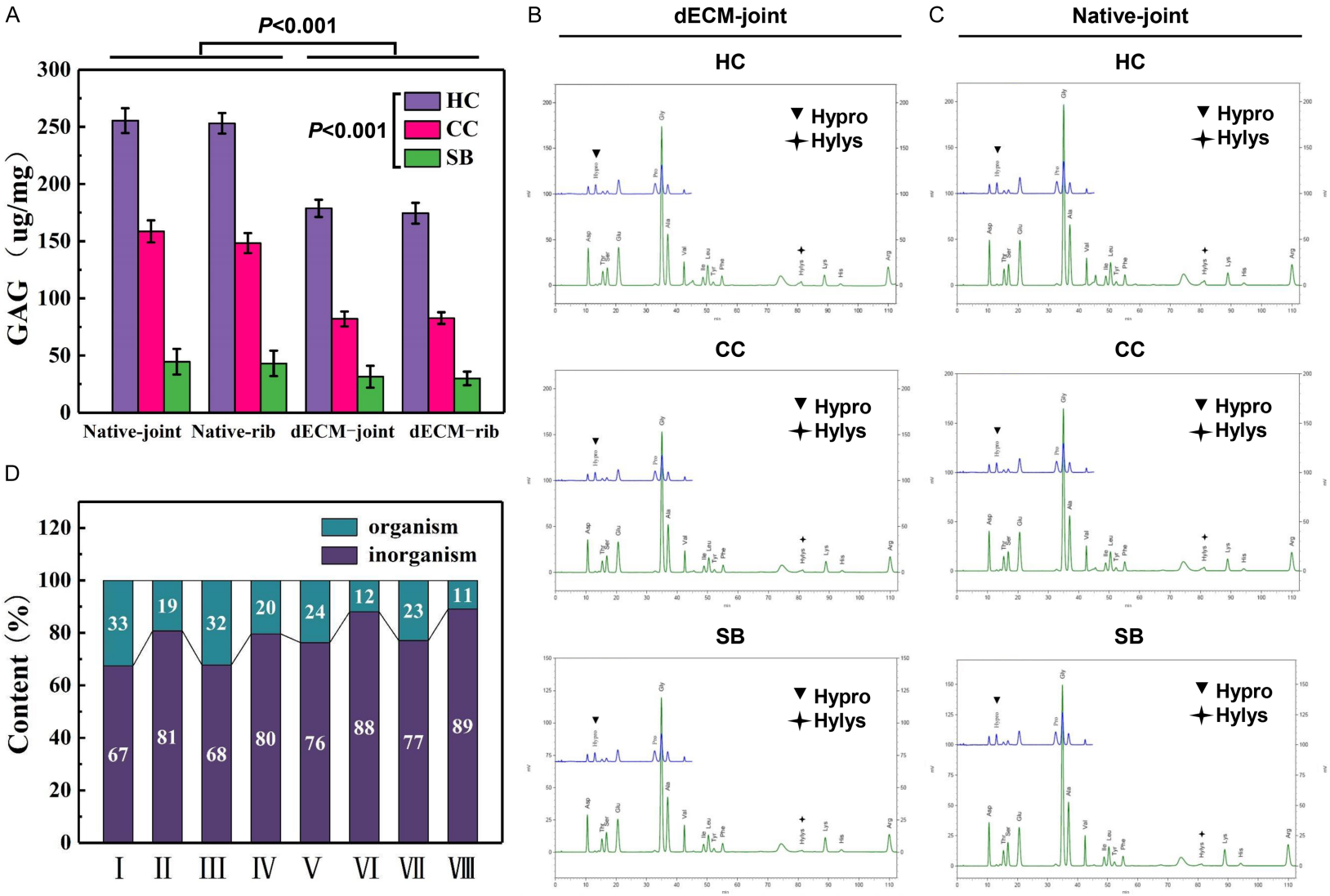
A
P<0.001
P<0.001
HC
CC
SB
GAG (ug/mg)
300
250
200
150
100
50
0
Native-joint
Native-rib
dECM−joint
dECM−rib
B
dECM-joint
C
Native-joint
HC
CC
SB
Hypro
Hylys
D
organism
inorganism
Content (%)
120
100
80
60
40
20
0
33
19
32
20
24
12
23
11
67
81
68
80
76
88
77
89
I
II
III
IV
V
VI
VII
VIII

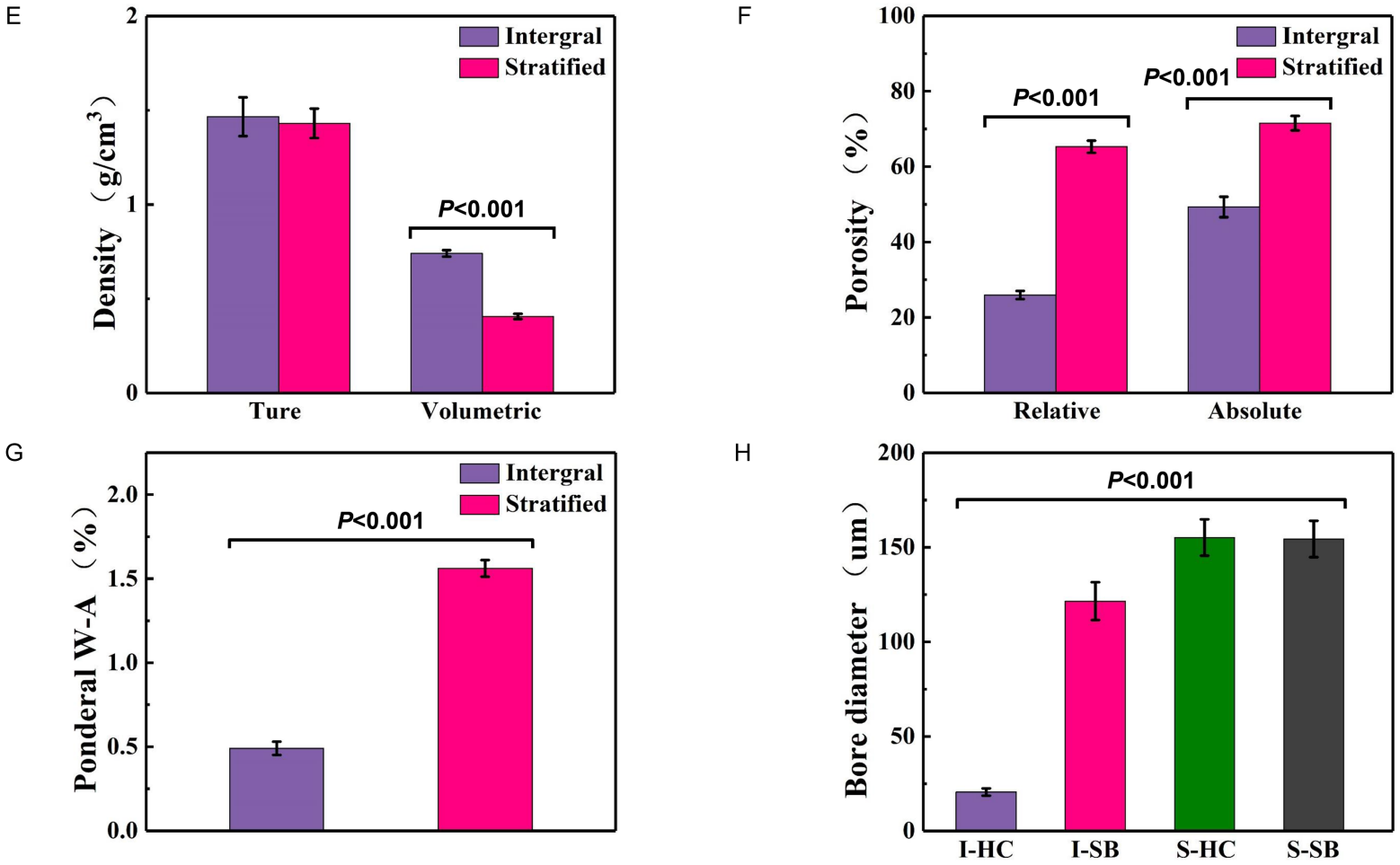


**Figure 5.** Detection of the components of the decellularized osteochondral matrix of joints and ribs. A. Glycosaminoglycan (GAG) content of decellularized joints and rib cartilage matrix. B, C. The amino acid content of the three-layer structure of HC, CC and SB in decellularized joints and rib cartilage. D. The content of organic and inorganic substances in the two-layer structure of natural and decellularized joints and rib cartilage (I: natural joint CC, II: natural joint SB, III: natural rib CC, IV: natural rib SB, V: decellularized joint CC, VI: decellularized joint SB, VII: decellularized rib CC, VIII: decellularized rib SB). E-H. Physical parameters of rabbit decellularized osteochondral integral scaffolds and layered scaffolds (true density and volume density, effective and absolute porosity, mass water absorption, cartilage and subchondral bone layer pore size).

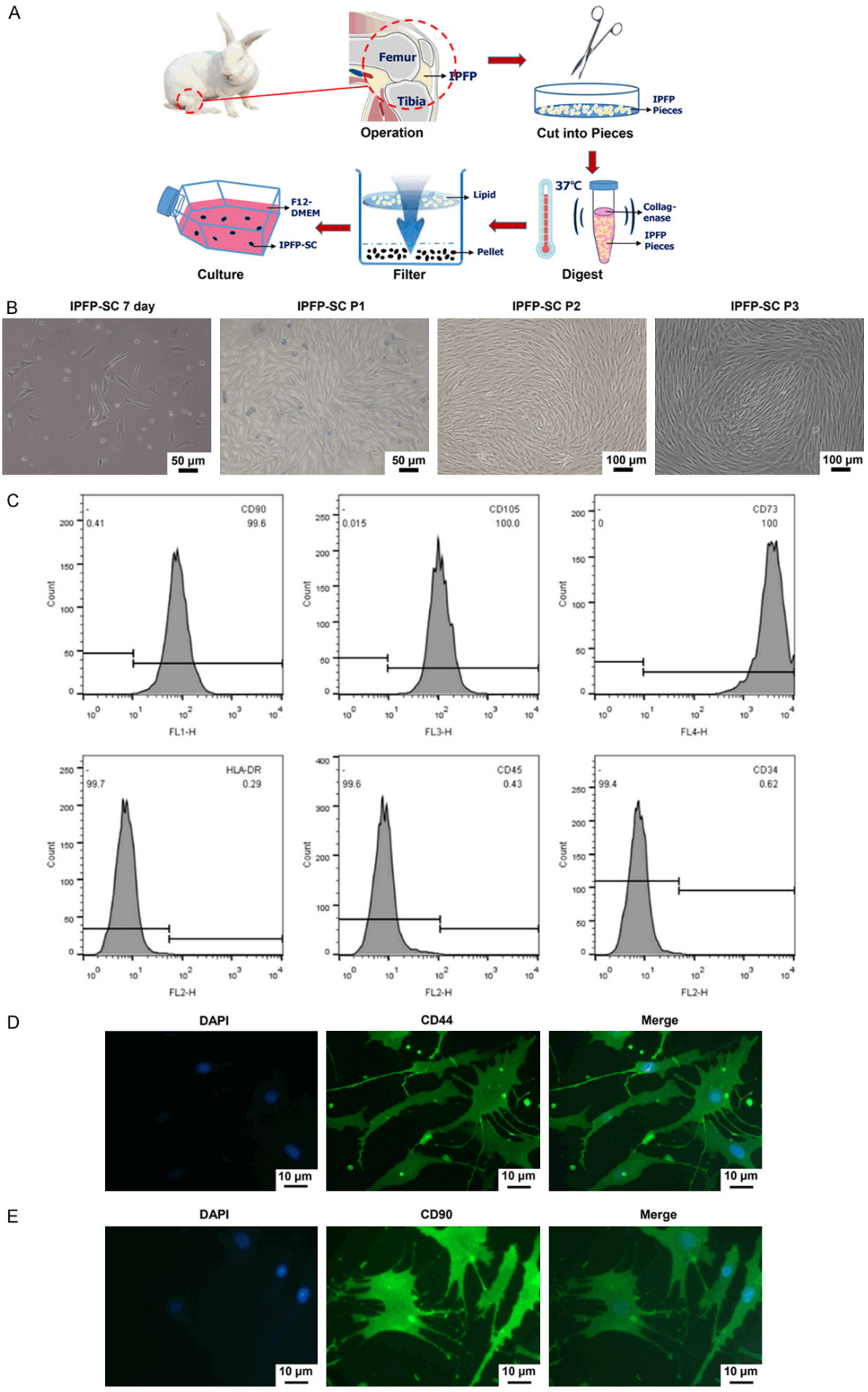
A
Femur
IPFP
Tibia
Operation
IPFP Pieces
Cut into Pieces
37℃
Collag-enase
IPFP Pieces
Digest
Lipid
Pellet
Filter
F12-DMEM
IPFP-SC
Culture
B
IPFP-SC 7 day
IPFP-SC P1
IPFP-SC P2
IPFP-SC P3
50 μm
50 μm
100 μm
100 μm
C
CD90
99.6
0.41
CD105
100.0
0.015
CD73
100
0
HLA-DR
0.29
99.7
CD45
0.43
99.6
CD34
0.62
99.4
Count
FL1-H
FL3-H
FL4-H
FL2-H
D
DAPI
CD44
Merge
10 μm
E
DAPI
CD90
Merge
10 μm

**Figure 6.** Isolation and identification of rabbit infrapatellar fat pad stem cells (IPFP-SCs). A. Schematic diagram of rabbit IPFP-SC extracted by collagenase digestion method. B. Morphology of rabbit IPFP-SC. C-E. Flow cytometry and immunofluorescence were used to identify molecular markers on the surface of IPFP-SC.

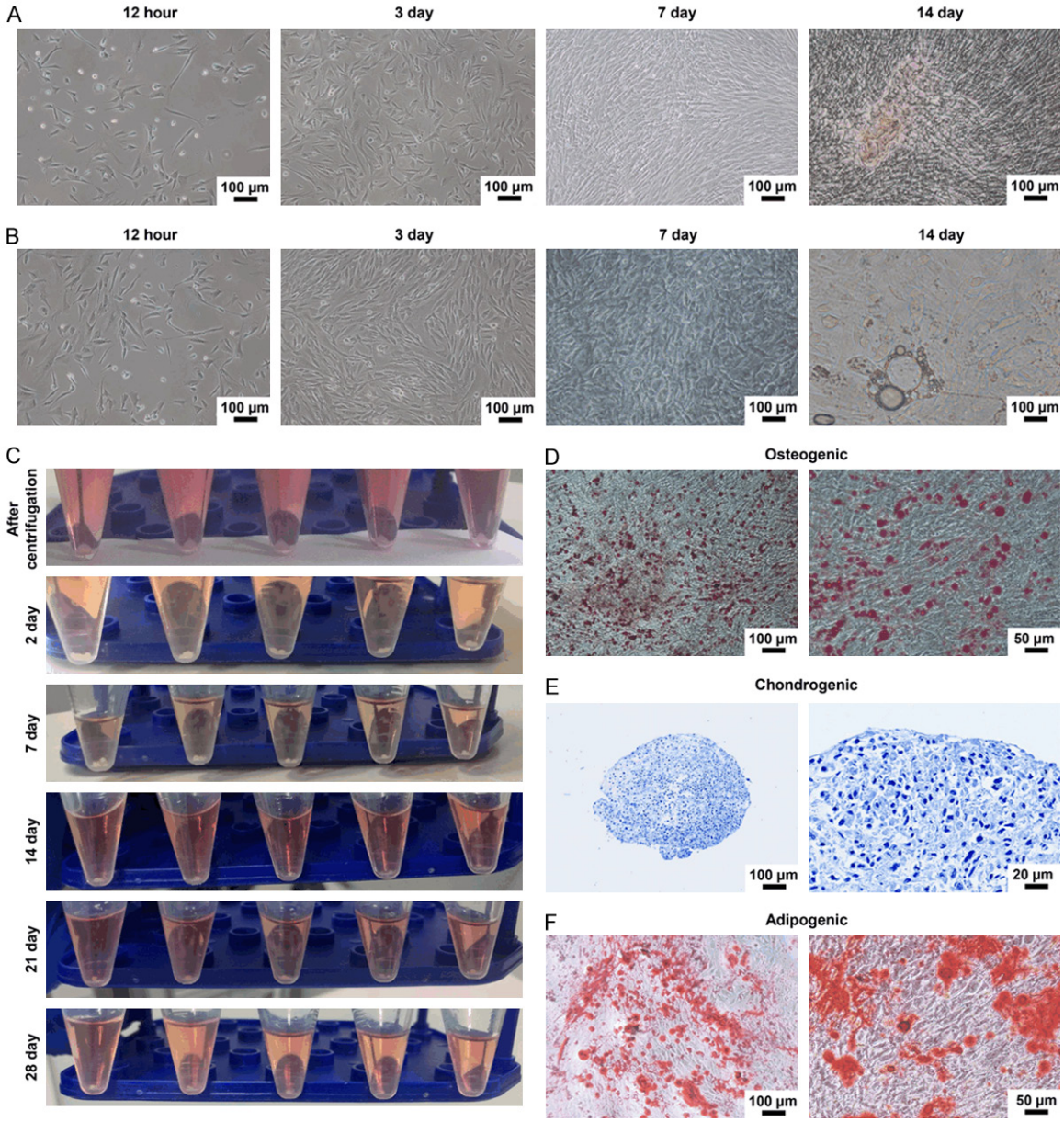


**Figure 7.** Osteogenesis, cartilage and adipogenesis of IPFP-SC. A. The morphology of rabbit IPFP-SC osteogenic differentiation. B. Morphology of adipogenic differentiation of rabbit IPFP-SCs. C. Rabbit IPFP-SC induced differentiation into cartilage. D. Alizarin red staining after osteogenic differentiation. E. Toluidine blue staining after chondrogenesis induced differentiation. F. Oil Red O staining image after adipogenesis induced differentiation.

sions of SOX9, ACAN, and COL2A1 were greatly upregulated in group C, I-HC, and S-HC. Similarly, ALP was upregulated in the dECM-SB group, and the expressions of SOX9, ACAN, and COL2A1 in the dECM-HC group were also upregulated ($P < 0.001$, **Figure 10B-E**).

*Decellularized matrix scaffold loaded with IPFP-SC repaired rabbit osteochondral defects*

To study the effect of a variety of decellularized matrix scaffolds loaded with IPFP-SC on repairing rabbit osteochondral defects, a rabbit fem-

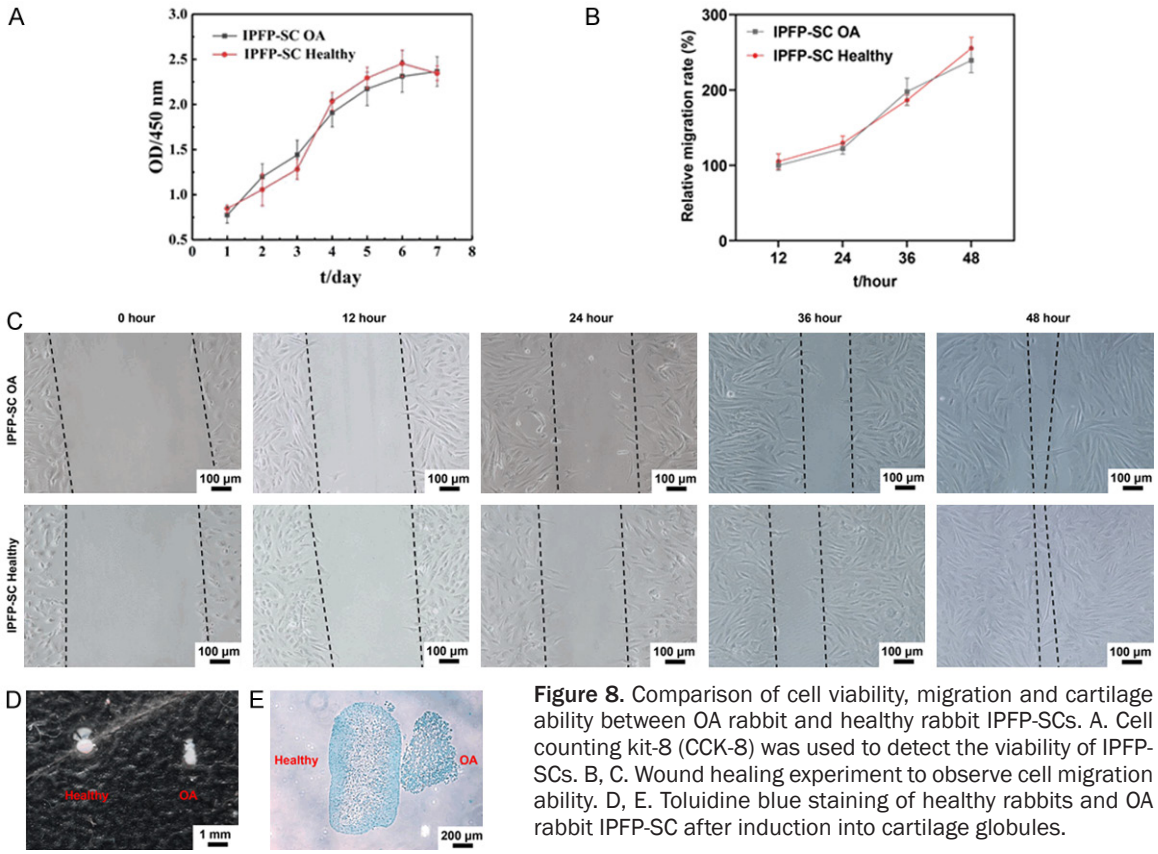


**Figure 8.** Comparison of cell viability, migration and cartilage ability between OA rabbit and healthy rabbit IPFP-SCs. A. Cell counting kit-8 (CCK-8) was used to detect the viability of IPFP-SCs. B, C. Wound healing experiment to observe cell migration ability. D, E. Toluidine blue staining of healthy rabbits and OA rabbit IPFP-SC after induction into cartilage globules.

oral trochlear osteochondral defect model was established (**Figure 11A**). Various decellularized osteochondral scaffolds were implanted into the osteochondral defect model, as shown in **Figure 11B-D**. After 6 months, the repairing effect of tissue engineering groups was better than that of blank group, and compared with the same type of scaffold, the effect of IPFP-SC loaded group was better than the simple scaffold group (**Figure 11E**). The histological staining results are shown in **Figure 12A-D**. The overall repair effect of the loaded IPFP-SC group showed a better effect than that of the stent alone group. The cartilage repair in the layered scaffold group was better than the whole scaffold group, but the result was the opposite in subchondral bone repair (**Figure 12A-D**).

## Discussion

OA is a highly complex disease [1]. During the development of OA, the CC connecting HC and SB will degenerate, straighten, and lose curvature and change the composition of the wet line bonding line [3, 22]. In these changes in composition and structure, HC and SB influences each other [23]. Therefore, the joint osteochondral should be treated as a whole in OA diagnosis and treatment.

Many researches used rib cartilage grafts to repair osteochondral defects [24, 25]. Volova et al. used allogeneic and autologous decalcified rabbit costal cartilage composite chondrocytes and transplanted them into the defect [26]. It was found that there was only a histological difference in the early stage, and the bone and cartilage could be better repaired [26]. Scholars such as Nishinaka employed autogenous costal cartilage transplantation to reconstruct the humeral head to treat advanced dissociative humeral capsular chondroitis [27]. No significant difference has been found in elbow function scores after surgery, and no patients showed obvious OA imaging changes in the later stage [27]. The above results suggested that rib HC can be used as an important source in cartilage tissue reconstruction engineering. Similarly, we did not detect significant difference between rib cartilage and articular cartilage in terms of structure or composition.

Additionally, we have completely removed cells and debris while retaining GAG, amino acids and other ingredients, and avoided the occur-

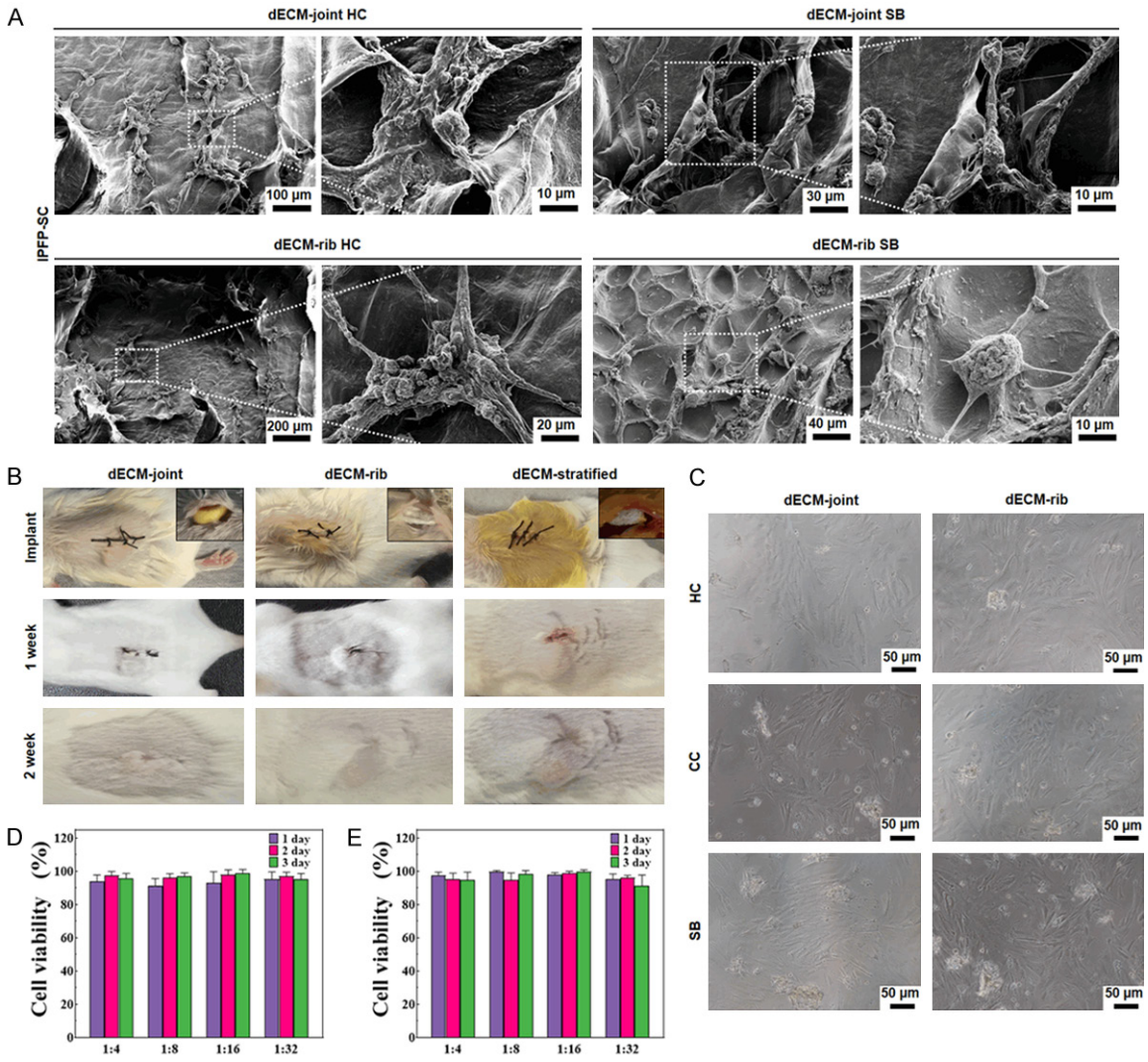


**Figure 9.** Detection of biocompatibility and biotoxicity of rabbit decellularized osteochondral matrix and scaffold. A. SEM scan of rabbit decellularized bone cartilage whole scaffold loaded with IPFP-SC. B. Decellularized joints and rib cartilage scaffolds were implanted subcutaneously in mice. C. Decellularized osteochondral granules were co-cultured with IPFP-SC. D, E. The IPFP-SC cell viability (%) in the extract of the joint and rib decellularized osteochondral scaffold was tested by CCK-8.

rence of immune inflammatory reactions to a great extent. Specifically, there was a loss of organic components after decellularization, and there was no significant difference in the amino acid content of Hypro and Hylys before or after decellularization, suggesting that the molecular structure of collagen will not be damaged during the decellularization process. In addition to supporting the framework, HAP and other inorganic components also have different functions in bone tissues, such as stimulating MSC osteogenic differentiation, repairing defective tissues, and osteoinduction and bone conduction effects [28, 29]. Interestingly, this method has almost no effect on inorganic substances during the decellularization process.

In bone and cartilage tissue engineering, ensuring the mechanical properties of the scaffold is one of the unsolved problems. Cheng et al. used CDM scaffolds to be cross-linked at a concentration of 0.05% genipin and inoculated with human ADSC for 4 weeks [30]. The results showed that the materials did not enhance cell adhesion or the production of new matrix [30]. Beck et al. applied pig DCC particles and methacrylic acid composite scaffold to

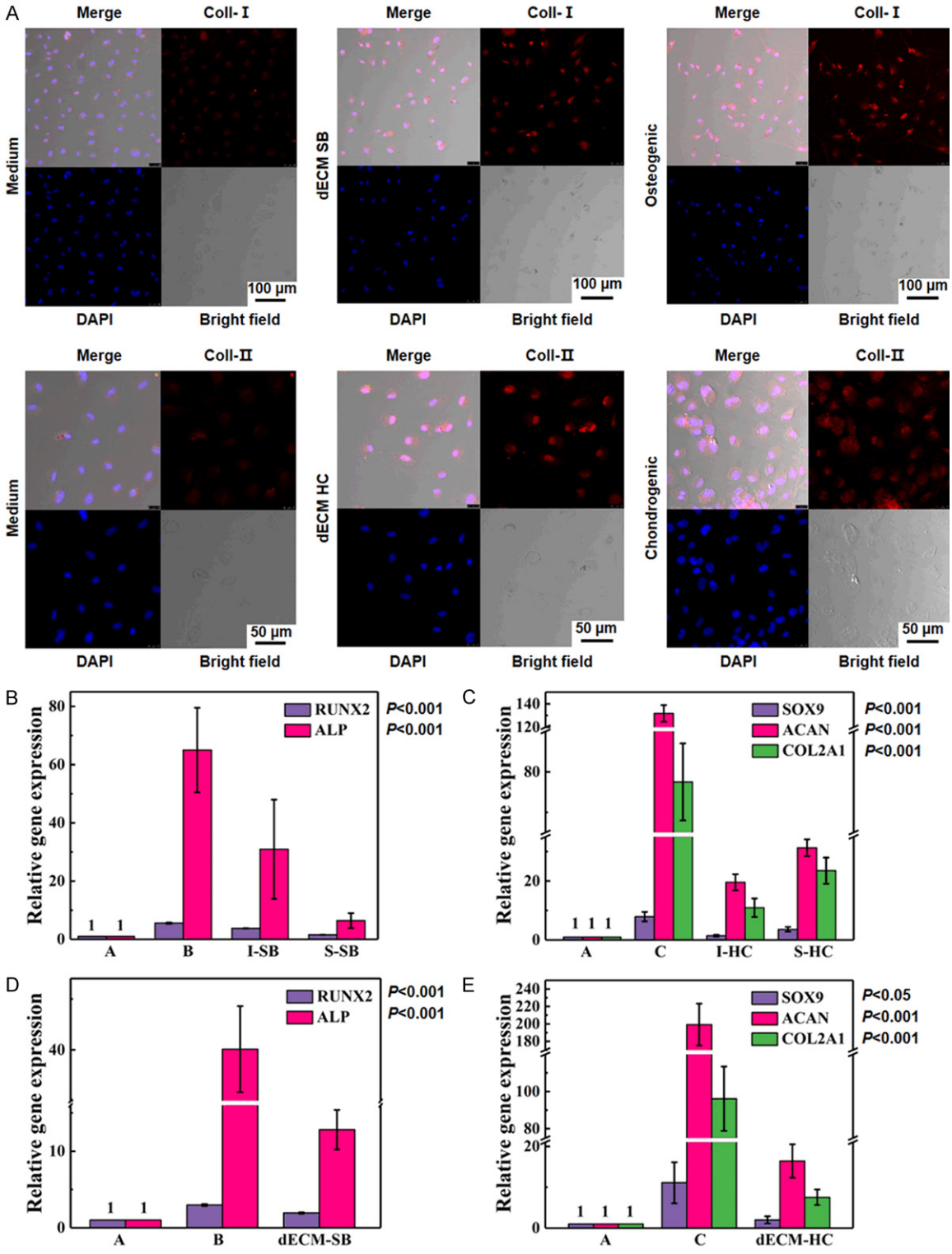


**Figure 10.** *In vitro* induction of rabbit decellularized osteochondral matrix and scaffold loaded with IPFP-SC. A. Immunofluorescence was used to determine the expressions of Coll-I and Coll-II. B, C. Real-time quantitative PCR (RT-qPCR) was used to determine the relative expressions of osteogenic cartilage genes after IPFP-SC stereo culture induction. A. Normal culture without inducing factors; B. Osteogenic induction liquid induction; C. Chondrogenic induction liquid induction; I-SB: Whole subchondral bone scaffold; S-SB: Layered subchondral bone scaffold; I-HC: Whole hyaline cartilage scaffold; S-HC: Layered hyaline cartilage scaffold. D, E. RT-qPCR was used to determine the relative expressions of osteogenic cartilage genes after co-culture of IPFP-SC decellularized particles. dECM-SB: co-cultured decellularized subchondral bone particles with IPFP-SC; dECM-HC: co-cultured decellularized hyaline cartilage particles with IPFP-SC.

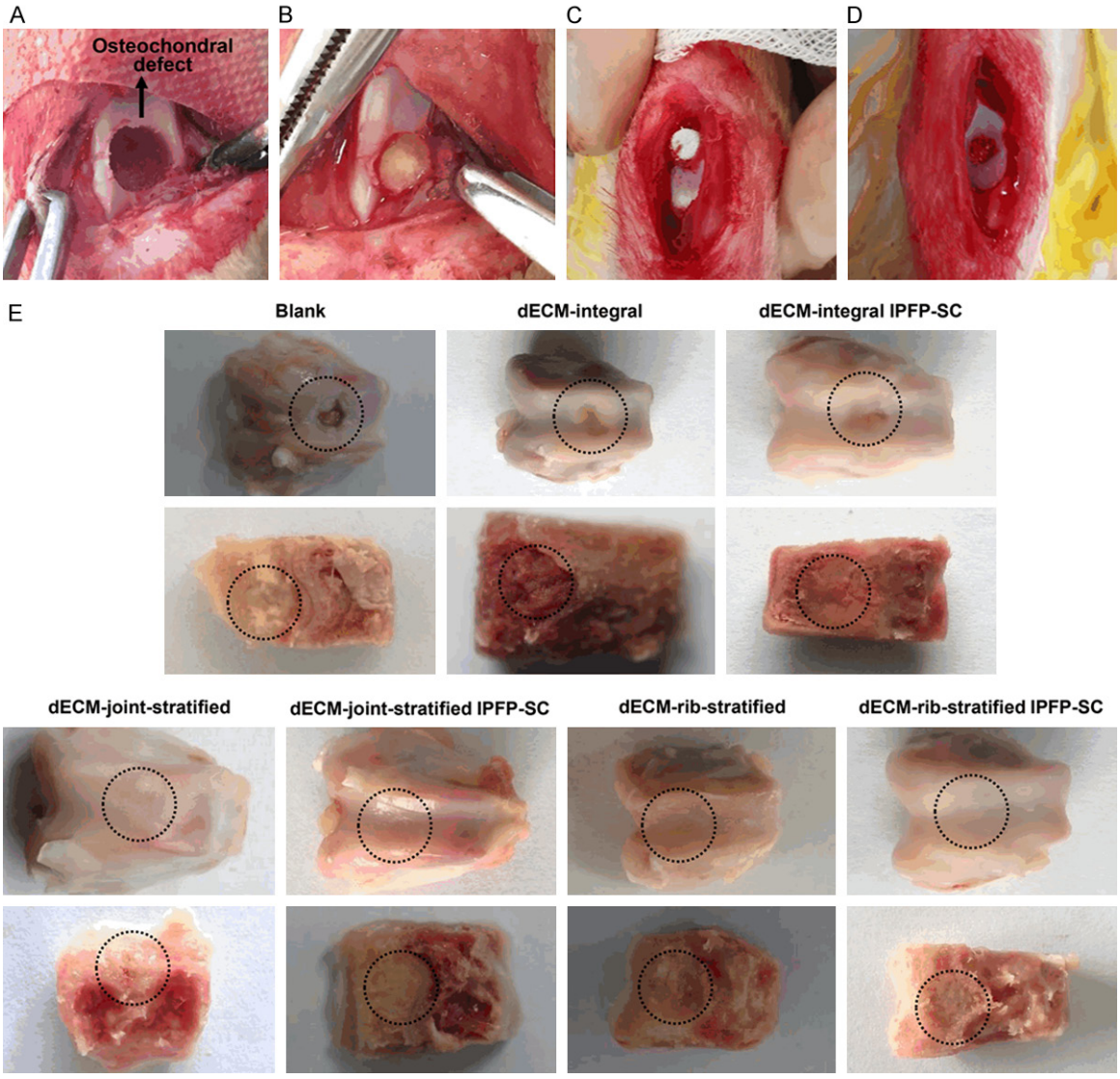


**Figure 11.** A variety of decellularized osteochondral scaffolds were implanted into the osteochondral defect model and postoperative treatment. A. Fabrication of osteochondral defect in the middle of the pulley. B. Decellularized whole osteochondral scaffold implantation. C. Decellularized layered osteochondral scaffold implantation. D. Decellularized layered osteochondral scaffold loaded with IPFP-SC implantation. E. Observation of gross specimen after repairing osteochondral defect 6 months. dECM: decellularized extracellular matrix.

embed mouse BMSC to form a hydrogel [31]. Their research showed that although the initial compression modulus was within 95% of the natural cartilage, the mechanical properties declined rapidly in the normal cartilage range within 6 weeks [31]. These studies have shown that using DCC or DVC scaffolds, mechanical properties of them cannot replace the mechanical properties of natural tissues. In this study, compared with normal osteochondral tissues, the acellular osteochondral scaffold showed increased stiffness and fragility, and reduced toughness. This may be due to the loss of more inorganic components such as collagen and GAG during the decellularization process, but there was almost no loss of inorganic components such as HAP or calcium phosphate. Thus, how to reconstruct and simulate the structure of natural osteochondral tissue, especially the ultrastructure, is also an important research direction in the future.

IPFP can play a role of liner, lubrication and cushioning the friction of articular cartilage sur-

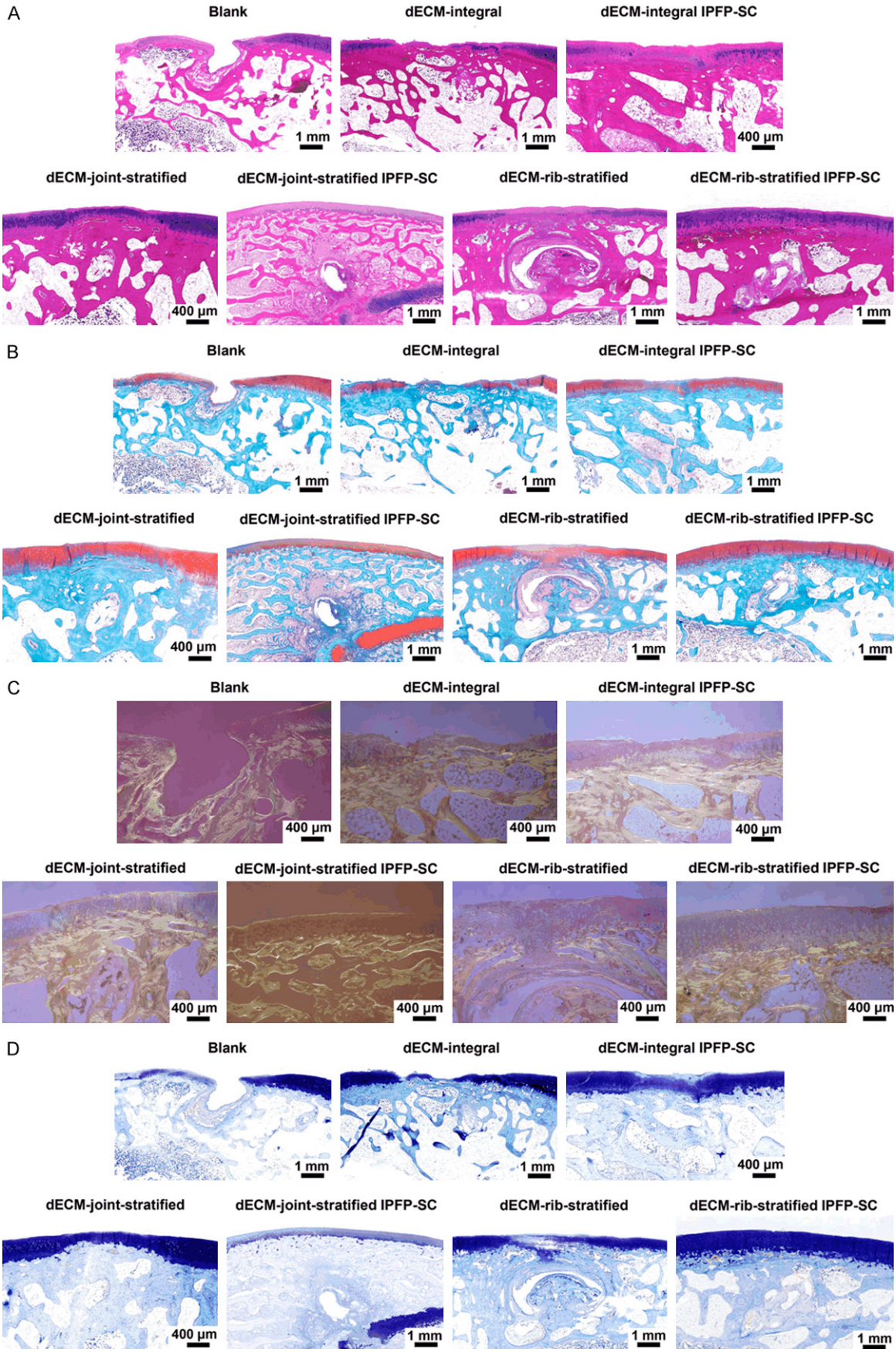
A
Blank
dECM-integral
dECM-integral IPFP-SC
dECM-joint-stratified
dECM-joint-stratified IPFP-SC
dECM-rib-stratified
dECM-rib-stratified IPFP-SC
B
Blank
dECM-integral
dECM-integral IPFP-SC
dECM-joint-stratified
dECM-joint-stratified IPFP-SC
dECM-rib-stratified
dECM-rib-stratified IPFP-SC
C
Blank
dECM-integral
dECM-integral IPFP-SC
dECM-joint-stratified
dECM-joint-stratified IPFP-SC
dECM-rib-stratified
dECM-rib-stratified IPFP-SC
D
Blank
dECM-integral
dECM-integral IPFP-SC
dECM-joint-stratified
dECM-joint-stratified IPFP-SC
dECM-rib-stratified
dECM-rib-stratified IPFP-SC

**Figure 12.** Histological observation of cartilage defect tissue repair specimens. A. HE staining image. B. Safranin solid green staining image. C. Stained image of Sirius. D. Toluidine blue staining image.

face in knee joint activities [32]. It can increase the area of the synovial membrane of the knee joint, promote the secretion of more synovial fluid, and the lipid droplets contained in it could also serve as a nutritional reserve for the knee joint [33]. Recent studies have shown that IPFP-SC has the strongest cartilage ability of different MSCs, followed by BM-SC, and SCF-SC showed the lowest ability [34, 35]. Wei et al. compared the IPFP-SC of patients with different BMI, and found no significant difference in the cartilage ability [36]. Moreover, they also compared IPFP between patients with OA and patients with anterior cruciate ligament injury during reconstruction, and found that both ADSCs had the same degree of downregulation in gene expressions of Coll-II and GAG, and that IPFP-infiltrated macrophages in multiple groups affected the expression of hyaline cartilage genes, suggesting that pro-inflammatory macrophages played a negative role in articular cartilage repair [36].

At present, there have been more *in vivo* studies using MSC for tissue engineering construction to repair osteochondral defects. Masuoka et al. implanted collagen scaffolds loaded with ADSCs into full-thickness cartilage defects in rabbit joints, and found that fibrocartilage was formed in the defects of the single scaffold group, while IHC in the ADSC group showed a high expression of Coll-II [37]. Yucel et al. inoculated ear cartilage defects and rat ADSCs together on the back of rats, and observed that ADSC composite transplantation increased the survival area and decreased cell apoptosis [38]. In this study, a whole or layered osteochondral scaffold made of a variety of acellular matrices was used to load IPFP-SC to repair rabbit osteochondral defects. We found that the repairing effect of all tissue engineering construction methods was better than natural repair. In comparison between the same kinds of decellularized osteochondral scaffolds, the repairing effect of loading IPFP-SC was better than the blank scaffold group. The decellularized rib cartilage-derived layered osteochondral scaffold showed no significant difference in gross specimen observation and slice histological staining when compared with the decellularized articular cartilage-derived scaffold. This suggested that rib cartilage can be used as a promising material source to replace joint osteochondral in OA therapies, providing new ideas for the acquisition of tissue engineering materials and the improvement of methods. The overall scaffold has been shown to be effective in repairing subchondral bone, possibly because it provided better bone conduction and osteoconduction. The layered scaffold has a stronger effect on repairing articular cartilage, which may be due to the greatly improved cell infiltration capacity compared with the cartilage integral scaffold, and the effective growth space and number of proliferative cells are increased. Thus, the decellularized extracellular matrix loaded with IPFP-SC has a strong repairing effect on rabbit osteochondral defects. However, there are some limitations in this study. The protein expression levels of RUNX2, ALP, SOX9, ACAN, and COL2A1 after co-culture of IPFP-SC decellularized particles need to be detected. Due to the small size of the New Zealand white rabbit, the lower limb force line is not as close to the human body as the large upright animal, and the area of osteochondral defect is small. Furthermore, there is no large area defect for comparative study. In addition, the future research should be focused on how to improve the mechanical properties of the stent.

In this study, we found that rib cartilage and joint osteochondral were similar in structure and tissue composition and may be used as an alternative source of materials for joint osteochondral tissue engineering. In addition, both the acellular osteochondral scaffold and IPFP SC have the ability to repair osteochondral defects, and the combination of the two has a better repairing effect. In this study, we used rabbit joints and rib-derived acellular matrix to prepare biological scaffolds, loaded with rabbit IPFP SC, and repaired rabbit joint osteochondral damage. It provided a new method for tissue engineering to repair osteochondral damage in the future.

## Acknowledgements

Three-year Action Plan for Talent Construction of Changzheng Hospital “Pyramid Talent Project” [2020CZJS218-5].

## Disclosure of conflict of interest

None.

**Address correspondence to:** Dr. Qirong Qian, Department of Joint Surgery and Orthopedic Medicine, Changzheng Hospital, Naval Medical University, No. 415 Fengyang Road, Huangpu District, Shanghai 200003, China. Tel: +86-021-81885639; E-mail: qianqirong_qqr@163.com

## References

[1] Nelson AE. Osteoarthritis year in review 2017: clinical. Osteoarthritis Cartilage 2018; 26: 319-325.
[2] Lieberthal J, Sambamurthy N and Scanzello CR. Inflammation in joint injury and post-traumatic osteoarthritis. Osteoarthritis Cartilage 2015; 23: 1825-1834.
[3] Goldring SR and Goldring MB. Changes in the osteochondral unit during osteoarthritis: structure, function and cartilage-bone crosstalk. Nat Rev Rheumatol 2016; 12: 632-644.
[4] Mapp PI and Walsh DA. Mechanisms and targets of angiogenesis and nerve growth in osteoarthritis. Nat Rev Rheumatol 2012; 8: 390-398.
[5] Makris EA, Gomoll AH, Malizos KN, Hu JC and Athanasiou KA. Repair and tissue engineering techniques for articular cartilage. Nat Rev Rheumatol 2015; 11: 21-34.
[6] Vinatier C and Guicheux J. Cartilage tissue engineering: from biomaterials and stem cells to osteoarthritis treatments. Ann Phys Rehabil Med 2016; 59: 139-144.
[7] Kwon H, Brown WE, Lee CA, Wang D, Paschos N, Hu JC and Athanasiou KA. Surgical and tissue engineering strategies for articular cartilage and meniscus repair. Nat Rev Rheumatol 2019; 15: 550-570.
[8] Pantelic MN and Larkin LM. Stem cells for skeletal muscle tissue engineering. Tissue Eng Part B Rev 2018; 24: 373-391.
[9] Dufrane D. Impact of age on human adipose stem cells for bone tissue engineering. Cell Transplant 2017; 26: 1496-1504.
[10] Loh QL and Choong C. Three-dimensional scaffolds for tissue engineering applications: role of porosity and pore size. Tissue Eng Part B Rev 2013; 19: 485-502.
[11] Bhattacharjee P, Kundu B, Naskar D, Kim HW, Maiti TK, Bhattacharya D and Kundu SC. Silk scaffolds in bone tissue engineering: an overview. Acta Biomater 2017; 63: 1-17.
[12] Hao Z, Song Z, Huang J, Huang K, Panetta A, Gu Z and Wu J. The scaffold microenvironment for stem cell based bone tissue engineering. Biomater Sci 2017; 5: 1382-1392.
[13] Taraballi F, Sushnitha M, Tsao C, Bauza G, Liverani C, Shi A and Tasciotti E. Biomimetic tissue engineering: tuning the immune and inflammatory response to implantable biomaterials. Adv Healthc Mater 2018; 7: e1800490.
[14] Crapo PM, Gilbert TW and Badylak SF. An overview of tissue and whole organ decellularization processes. Biomaterials 2011; 32: 3233-3243.
[15] Yao Q, Zheng YW, Lan QH, Kou L, Xu HL and Zhao YZ. Recent development and biomedical applications of decellularized extracellular matrix biomaterials. Mater Sci Eng C Mater Biol Appl 2019; 104: 109942.
[16] Taylor DA, Sampaio LC, Ferdous Z, Gobin AS and Taite LJ. Decellularized matrices in regenerative medicine. Acta Biomater 2018; 74: 74-89.
[17] Bejleri D and Davis ME. Decellularized extracellular matrix materials for cardiac repair and regeneration. Adv Healthc Mater 2019; 8: e1801217.
[18] Lee JS, Choi YS and Cho SW. Decellularized tissue matrix for stem cell and tissue engineering. Adv Exp Med Biol 2018; 1064: 161-180.
[19] Wang Z, Li Z, Li Z, Wu B, Liu Y and Wu W. Cartilaginous extracellular matrix derived from decellularized chondrocyte sheets for the reconstruction of osteochondral defects in rabbits. Acta Biomater 2018; 81: 129-145.
[20] Wang Z, Han L, Sun T, Ma J, Sun S, Ma L and Wu B. Extracellular matrix derived from allogenic decellularized bone marrow mesenchymal stem cell sheets for the reconstruction of osteochondral defects in rabbits. Acta Biomater 2020; 118: 54-68.
[21] Rameshbabu AP, Ghosh P, Subramani E, Bankoti K, Kapat K, Datta S, Maity PP, Subramanian B, Roy S, Chaudhury K and Dhara S. Investigating the potential of human placenta-derived extracellular matrix sponges coupled with amniotic membrane-derived stem cells for osteochondral tissue engineering. J Mater Chem B 2016; 4: 613-625.
[22] Zarka M, Hay E, Ostertag A, Marty C, Chappard C, Oudet F, Engelke K, Laredo JD and Cohen-Solal M. Microcracks in subchondral bone plate is linked to less cartilage damage. Bone 2019; 123: 1-7.
[23] Lories RJ and Luyten FP. The bone-cartilage unit in osteoarthritis. Nat Rev Rheumatol 2011; 7: 43-49.
[24] Du D, Sugita N, Liu Z, Moriguchi Y, Nakata K, Myoui A and Yoshikawa H. Repairing osteochondral defects of critical size using multiple costal grafts: an experimental study. Cartilage 2015; 6: 241-251.
[25] Du D, Hsu P, Zhu Z and Zhang C. Current surgical options and innovation for repairing articu-

lar cartilage defects in the femoral head. J Orthop Translat 2020; 21: 122-128.
[26] Volova LT, Kotel'nikov GP, Lartsev IuV, Dolgushkin DA, Boltovskaia VV and Terterian MA. Peculiarities of regenerative processes after the plasty of osteochondral defects with combined cell-tissue grafts on the basis of autologous and allogeneic cell cultures from costal cartilage tissue. Morfologiia 2014; 146: 47-52.
[27] Nishinaka N, Tsutsui H, Yamaguchi K, Uehara T, Nagai S and Atsumi T. Costal osteochondral autograft for reconstruction of advanced-stage osteochondritis dissecans of the capitellum. J Shoulder Elbow Surg 2014; 23: 1888-1897.
[28] Matsusaki M, Kadowaki K, Tateishi K, Higuchi C, Ando W, Hart DA, Tanaka Y, Take Y, Akashi M, Yoshikawa H and Nakamura N. Scaffold-free tissue-engineered construct-hydroxyapatite composites generated by an alternate soaking process: potential for repair of bone defects. Tissue Eng Part A 2009; 15: 55-63.
[29] Ma B, Han J, Zhang S, Liu F, Wang S, Duan J, Sang Y, Jiang H, Li D, Ge S, Yu J and Liu H. Hydroxyapatite nanobelt/polylactic acid Janus membrane with osteoinduction/barrier dual functions for precise bone defect repair. Acta Biomater 2018; 71: 108-117.
[30] Cheng NC, Estes BT, Young TH and Guilak F. Genipin-crosslinked cartilage-derived matrix as a scaffold for human adipose-derived stem cell chondrogenesis. Tissue Eng Part A 2013; 19: 484-496.
[31] Beck EC, Barragan M, Tadros MH, Gehrke SH and Detamore MS. Approaching the compressive modulus of articular cartilage with a decellularized cartilage-based hydrogel. Acta Biomater 2016; 38: 94-105.
[32] Eymard F and Chevalier X. Inflammation of the infrapatellar fat pad. Joint Bone Spine 2016; 83: 389-393.
[33] Stephen JM, Sopher R, Tullie S, Amis AA, Ball S and Williams A. The infrapatellar fat pad is a dynamic and mobile structure, which deforms during knee motion, and has proximal extensions which wrap around the patella. Knee Surg Sports Traumatol Arthrosc 2018; 26: 3515-3524.
[34] Harrell CR, Markovic BS, Fellabaum C, Arsenijevic A and Volarevic V. Mesenchymal stem cell-based therapy of osteoarthritis: current knowledge and future perspectives. Biomed Pharmacother 2019; 109: 2318-2326.
[35] Garcia J, Mennan C, McCarthy HS, Roberts S, Richardson JB and Wright KT. Chondrogenic potency analyses of donor-matched chondrocytes and mesenchymal stem cells derived from bone marrow, infrapatellar fat pad, and subcutaneous fat. Stem Cells Int 2016; 2016: 6969726.
[36] Wei W, Rudjito E, Fahy N, Verhaar JA, Clockaerts S, Bastiaansen-Jenniskens YM and van Osch GJ. The infrapatellar fat pad from diseased joints inhibits chondrogenesis of mesenchymal stem cells. Eur Cell Mater 2015; 30: 303-314.
[37] Masuoka K, Asazuma T, Hattori H, Yoshihara Y, Sato M, Matsumura K, Matsui T, Takase B, Nemoto K and Ishihara M. Tissue engineering of articular cartilage with autologous cultured adipose tissue-derived stromal cells using atelocollagen honeycomb-shaped scaffold with a membrane sealing in rabbits. J Biomed Mater Res B Appl Biomater 2006; 79: 25-34.
[38] Yucel E, Alagoz MS, Eren GG, Yasar EK, Izmirli HH, Duruksu G, Isgoren S, Muezzinoglu B and Karaoz E. Use of adipose-derived mesenchymal stem cells to increase viability of composite grafts. J Craniofac Surg 2016; 27: 1354-1360.